Theory of the SrTiO₃ surface state two-dimensional electron gas

Guru Khalsa and A. H. MacDonald

Department of Physics, University of Texas at Austin, Austin, Texas 78712-1081, USA

We present a theory of the quasi-two-dimensional electron gas (2DEG) systems that appear near the surface of SrTiO₃ when a large external electric field attracts carriers to the surface. We find that nonlinear and nonlocal screening by the strongly polarizable SrTiO₃ lattice plays an essential role in determining 2DEG properties. The electronic structure always includes weakly bound bulklike bands that extend over many SrTiO₃ layers. At 2D carrier densities exceeding $\sim 10^{14}$ cm^{-2}, tightly bound bands emerge that are confined within a few layers of the surface.

I. INTRODUCTION

Two-dimensional electron gases can be formed in SrTiO₃ crystals[1–3] by gating,[4–6] by forming an interface with a polar perovskite,[1,3,7,8] or by placing a δ-doped[9] layer inside a bulk crystal. Although 2D electronic systems at LaAlO₃/SrTiO₃ interfaces have received particular attention,[7,8] there has also been important progress with other material systems.[10] SrTiO₃ two-dimensional electron gases (2DEGs) appear to be strongly correlated when their thermodynamics is probed capacitively[11] and exhibit both superconductivity[12] and magnetism,[13] sometimes simultaneously.[14] There is at present only a very primitive understanding of the measured properties of these potentially interesting 2DEG systems. The current paper is motivated by the view that progress can be accelerated by the development of concrete microscopic models that are simplified relative to full *ab initio* electronic structure calculations,[15–18] allowing electric properties to be estimated easily and compared with experiment.

In this paper, we present a model of SrTiO₃ 2DEGs that is partly phenomenological and simplified, but still sufficiently realistic to be predictive. We focus on electrostatically gated surface 2DEGs, although our approach applies without much change to the case of interface-confined systems. The same model is readily adapted to describe δ-doped 2DEGs inside the STO bulk, STO 2DEGs that are modulated by a back gate, and 2DEGs in other d^0 systems, for example KTaO₃. The model assumes that the itinerant electronic degrees of freedom are derived from the SrTiO₃ t_{2g} bands. We use a nearest-neighbor tight-binding model to describe hopping between TiO₂ planes and either tight-binding or $\vec{k} \cdot \vec{p}$ models to describe wave-function variation within TiO₂ planes. The strength of interplane hopping parameters, and the values of the heavy and light masses within planes are estimated on the basis of recent ARPES[19] and bulk magnetic oscillation[20] experimental results. Some aspects of the 2DEG electronic structure are sensitive to the influences of spin-orbit coupling and SrTiO₃'s low-temperature tetragonal distortion on the host material's conduction band, even at the highest 2D carrier densities.

The extremely strong dielectric response of the SrTiO₃ lattice plays a key role in our model at all carrier densities. Our main results are summarized in Fig. 1. We conclude that unless vertically confined on both sides by vacuum or insulating tunnel barriers, SrTiO₃ 2DEGs spread across a large number of TiO₂ planes. This property is a direct consequence of the host

material's very large linear dielectric constant, which weakens confinement, and occurs in spite of relatively large carrier masses which favor confinement. At high carrier densities, and hence large electric fields, dielectric screening saturates and the 2DEG is mostly confined to the first few TiO₂ planes. However, a portion of the 2DEG, making a contribution to the 2D density that is approximately fixed in absolute terms, still spills over many layers. This low-density weakly confined part of the 2DEG can make an important contribution to some 2DEG properties.

Our paper is organized as follows. In the following section, we provide a detailed explanation of the model that we use. We have identified three different density regimes for SrTiO₃ surface-bound 2DEGs. In Secs. III–V, we characterize the nature of the 2DEG electronic structure in low ($n < 1 \times 10^{14}$ cm^{-2}), mid (1×10^{14} cm$^{-2} < n < 5 \times 10^{14}$ cm^{-2}), and high ($n > 5 \times 10^{14}$ cm^{-2}) 2DEG carrier density regimes, respectively. Finally, in Sec. VI, we summarize our results and speculate on the types of electronic properties that might be achievable in SrTiO₃ 2DEG systems.

II. MODEL

A. t_{2g} tight-binding model

SrTiO₃ is a nonpolar pseudocubic band insulator with an electronic gap of $\sim$3.2 eV separating its oxygen *p*-orbital dominated valance band, from its Ti t_{2g}-orbital dominated conduction band. The Ti e_g bands are split by the crystal field and pushed up in energy by $\sim$2 eV (see Ref. 21) relative to the t_{2g} bands and are therefore neglected in our model. The conduction band minimum is at the Γ point. The bulk t_{2g} bands are split at the Γ point, in the first place by spin-orbit interactions, which push one time-reversed pair of t_{2g} bands up by $\sim$18 meV relative to the other two pairs. The two lower-energy bands are further split below 110 K by a rotation of the octahedral oxygen environment, which is responsible for a tetragonal distortion.[22]

The starting point for any phenomenological description of the electronic structure of SrTiO₃ 2DEGs is an accurate representation of the bulk material electronic structure. Although this material has been studied for many years, its conduction band minimum was until recently not characterized with an accuracy sufficient to model low-carrier density 2DEGs. To remedy this, Allen *et al.* conducted[20] magnetotransport studies

on a series of low-density electron-doped MBE-grown samples of SrTiO$_3$ in fields up to 31 T and fit a six band $\mathbf{k} \cdot \mathbf{p}$ model of the Ti t_{2g} bands to the magnetic oscillation data. The bulk band parameters used here have been taken from that study. These experiments suggest that in the absence of spin-orbit coupling the tetragonal distortion at 4 K would push the xy bands up by $\sim$3.2 meV relative to yz and zx bands. Together the two-corrections fully lift the t_{2g} manifold degeneracy, even in the bulk. [Because of orbital mixing, the spin-orbit (SO) splitting and tetragonal splitting parameters do not directly correspond to the Γ point band energies.]

Although the p-d oxygen bonding and e_g antibonding orbitals do not explicitly enter our model, they do appear

implicitly in the form of the Hamiltonian. Consider, for example, hopping between a Ti xy orbital and its neighboring oxygens within a TiO$_2$ plane [see Fig. 2(a)]. Along the x direction, the dominant bonding is π_{pd} through the O-p_y orbital and along the y direction, π_{pd} through the O-p_x orbital. Overlap with other O-p orbitals is small by symmetry. This rule is preserved througout the Ti-O-Ti bonding network. For the Ti-yz orbital, π_{pd} bonding dominates along the y direction through O-p_z orbitals. Bonding along the x direction vanishes in a Slater-Koster two-center approximation and is weak. Temporarily ignoring the spin-orbit and tetragonal distortion effects, these observations suggests a tight-binding model for a single isolated layer of the form

$$
H_\sigma^{\mathrm{SL}} = \begin{pmatrix} -2t'\cos(k_x) - 2t\cos(k_y) & 0 & 0 \\ 0 & -2t\cos(k_x) - 2t'\cos(k_y) & 0 \\ 0 & 0 & -2t\cos(k_x) - 2t\cos(k_y) \end{pmatrix} \begin{Bmatrix} yz,\sigma \\ zx,\sigma \\ xy,\sigma \end{Bmatrix}, \qquad (1)
$$

where the cubic lattice constant is used as a length unit, the metal lattice site energies are used as the zero of energy, t quantifies the dominant π_{pd} bonding process, and t' describes the weaker bonding process. The column on the right specifies the orbital representation used for this Hamiltonian matrix. Hopping terms that couple different t_{2g} orbitals are allowed[23] from a symmetry point of view. However, Allen *et al.* were unable to distinguish this mixing parameter from zero in their recent analysis of SdH data.[20] We therefore ignore these processes in our model. For lower-carrier densities, it is sometimes convenient to use a simplified version of this model in which we expand Eq. (1) around the 2D Γ point. We find that for 2D wave vectors that are small compared to Brillouin zone dimensions,

$$
H_\sigma^{SL} = \begin{pmatrix} \epsilon_{yz,0} + t'k_x^2 + tk_y^2 & 0 & 0 \\ 0 & \epsilon_{zx,0} + tk_x^2 + t'k_y^2 & 0 \\ 0 & 0 & \epsilon_{xy,0} + tk_x^2 + tk_y^2 \end{pmatrix} \begin{Bmatrix} yz,\sigma \\ zx,\sigma \\ xy,\sigma \end{Bmatrix}, \qquad (2)
$$

where $\epsilon_{yz,0} = \epsilon_{zx,0} = -2t - 2t'$ and $\epsilon_{xy,0} = -4t$. We use this low-density form for the planar Hamiltonian for most of the calculations presented below. The more general tight-binding model must be used when 2D carrier densities are large and confinement is strong and can be adopted when required without essential complication.

In the same representation, adjacent 2D layers are coupled by an interlayer hopping term of the form

$$
H_\sigma^C = \begin{pmatrix} t & 0 & 0 \\ 0 & t & 0 \\ 0 & 0 & t' \end{pmatrix} \begin{Bmatrix} yz,\sigma \\ zx,\sigma \\ xy,\sigma \end{Bmatrix}. \qquad (3)
$$

Here, the symmetry of the bonding network has again been employed to note that the xy orbital has the weaker interlayer coupling, t'. Because t' is expected to be substantially smaller than t, the xy bands in single-layer 2DEGs are pulled down by $\sim 2t$ at the Γ point relative to the yz and zx bands. In the bulk limit, on the other hand, the three bands are degenerate because each has two strong hopping and one weak hopping direction. Any amount of confinement in the $\hat{z}$ direction pushes the bottom of the $\{yz,zx\}$ bands up relative to the xy band and leads to orbital polarization.

For low-carrier densities, on-site ($\boldsymbol{k}$-independent) terms due to tetragonal distortions and spin-orbit coupling must be included.[23] The tetragaonal distortion is represented by a

parameter Δ_T which characterizes the difference in site energy between xy and $\{yz,zx\}$-orbitals and spin-orbit coupling by an interaction strength parameter Δ_{SO}. The distortion Hamiltonian is

$$
T_\sigma = \begin{pmatrix} 0 & 0 & 0 \\ 0 & 0 & 0 \\ 0 & 0 & \Delta_T \end{pmatrix} \begin{Bmatrix} yz,\sigma \\ zx,\sigma \\ xy,\sigma \end{Bmatrix}, \qquad (4)
$$

and the spin-orbit Hamiltonian, modeled in an atomic approximation, is

$$
H^{\mathrm{SO}} = \frac{\Delta_{\mathrm{SO}}}{3} \begin{pmatrix} 0 & i & 0 & 0 & 0 & -1 \\ -i & 0 & 0 & 0 & 0 & i \\ 0 & 0 & 0 & 1 & -i & 0 \\ 0 & 0 & 1 & 0 & -i & 0 \\ 0 & 0 & i & i & 0 & 0 \\ -1 & -i & 0 & 0 & 0 & 0 \end{pmatrix} \begin{Bmatrix} yz,\uparrow \\ zx,\uparrow \\ xy,\uparrow \\ yz,\downarrow \\ zx,\downarrow \\ xy,\downarrow \end{Bmatrix}. \qquad (5)
$$

Our model for the electronic structure of SrTiO$_3$ 2DEGs combines the single-particle model explained above with a Hartree approximation for electron-electron interactions. The external electric field, which produces surface confinement, is screened by carriers and by lattice relaxations of the partially ionic SrTiO$_3$ crystal. In SrTiO$_3$ lattice screening is strong and nonlinear and plays a subtle and essential role in confinement.
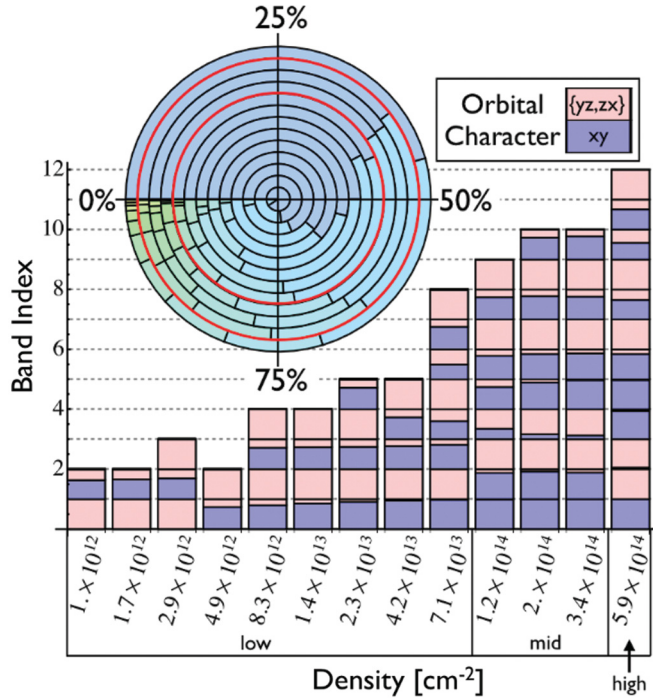
FIG. 1. (Color online) Orbital character at $k_\perp = 0$ of occupied doubly degenerate 2D subbands for a series of total areal densities. The xy and $\{yz,zx\}$ fractions in the orbital character of each band are represented by light blue and light red shading, respectively, and the band indices are ordered from lowest energy to highest. Both spin-orbit interactions and tetragonal splitting have been included in the band-structure model. The percentage of the total density associated with a given subband is summarized in the inset pie chart in which the rings from inside to outside correspond to the density values from lowest to highest. Individual band contributions for a particular density are ordered lowest energy to highest in a clockwise direction. The red lines in the pie chart separate the low, mid, and high density regimes identified in the text. At the highest total densities, most electrons occupy a small number of strongly confined bands.

B. Lattice relaxation model

The exceptionally strong and temperature-dependent linear dielectric response of bulk SrTiO₃ is associated with a soft optical phonon mode in which positively charged Sr and Ti atoms move in opposition to the negatively charged oxygen
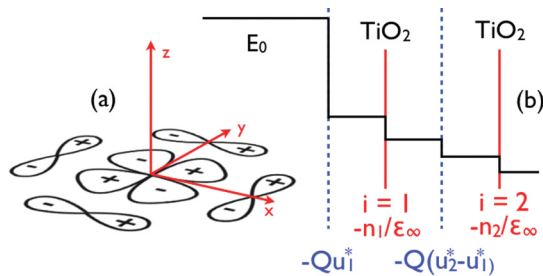

FIG. 2. (Color online) (a) p-d bonding network for Ti-xy orbital. The dominant bonding is in-plane π_{pd}, while the out-of-plane bonding is weak. (b) Schematic representation of the electric field drop in our model due to lattice (dashed blue) and electronic (solid red) screenings. Numerical factors have been dropped.

octahedra. Displacement of this mode in response to an external electric field produces screening. Because the mode is extremely soft only near the center of the Brillouin zone,[24] it responds strongly only when a large external field persists over several TiO₂ layers. In addition, this screening response is very nonlinear, saturating at very large electric fields. Since the reduction in electric field is proportional to the phonon mode displacement, saturation occurs because the phonon mode is anomalously soft only for small displacements.[24] In an attempt to capture this behavior qualitatively, we use a simple model of lattice relaxation which focuses on the soft-mode only. We write the lattice energy as

$$U = \frac{1}{2}\sum_{i,j} u_i K_{i,j} u_j - Q\sum_i E_i u_i + \frac{\gamma}{4}\sum_i u_i^4, \quad (6)$$

where u_i is the displacement of the soft mode on the ith lattice site, E_i is the average electric field in the ith cell, Q is an effective charge defined in terms of the polarization density per unit soft-mode displacement, and γ is a parameter chosen to capture the nonlinearity of the dielectric response as discussed further below. Here, $K_{i,j} = K_{i-j}$ is the dynamical matrix at 2D wave vector $q_\perp = 0$. We fit K_{ij} to the soft-mode phonon dispersion using a form with a local on-site contribution and a Gaussian nonlocal contribution. In momentum space, this takes the form

$$K(q,G) = (2\pi)^2 \mu \left[f_0^2 - f_1^2 e^{-\frac{\alpha_1^2}{2}(q+G)^2} - f_2^2 e^{-\frac{\alpha_2^2}{2}(q+G)^2} \right], \quad (7)$$

where q is the lattice momentum, G is a reciprocal lattice vector, and $\mu = 24$ amu is the appropriate reduced mass for the Ti atom moving opposite the oxygen octahedra. The parameters f_0, the strength of the on-site term, and f_1 and α_1 were chosen to reproduce the measured phonon dispersion. f_2 and α_2 have been chosen to fit the low temperature dielectric response and agree well with the low temperature phonon dispersion.[25] By minimizing Eq. (6) in the absence of an electric field and evaluating Eq. (7) at $q = 0$, we find that

$$\gamma = \left[\frac{2\pi(f_0 - f_1 - f_2)}{u_{\text{NL}}} \right]^2, \quad (8)$$

where u_{NL} is the mode displacement at which nonlinear dielectric response is seen. (See the discussion below).

Because the relative displacements of all atoms are known, only a single displacement coordinate, u_i, is needed to describe the response of the unit cell to perturbations along the principle crystal axes. Given the electric field in each cell of the crystal, Eq. (6) can be minimized to find the appropriate set of displacements, $\{u_i^*\}$. We define the three-dimensional polarization density of the SrTiO₃ as

$$P_i = \frac{1}{a^3} Q u_i^* \left[\Theta(z_i - a/2) - \Theta(z_i + a/2) \right], \quad (9)$$

where z_i is the location of the TiO₂ layer of interest, a is the lattice constant of the crystal, and $\Theta(z)$ in the Heaviside function. The precise way in which the polarization density is mapped onto our lattice model is immaterial on length scales larger than a lattice constant. To find the effective charge

TABLE I. Parameters used in the current study. The electronic structure parameters have been taken from Ref. [20], while ϵ_∞, ϵ_1, and ϵ_0 were taken from Refs. [24] and [27].

Model parameters		
Lattice constant	a	3.904 Å
Electronic parameters	t	236 meV
	t'	35 meV
	Δ_{SO}	18 meV
	Δ_T	3.2 meV
Dielectric response	ϵ_0	24408
	ϵ_1	1340
	ϵ_∞	5.5
	Q	$8.33e$
	u_{NL}	0.0034 Å
Dynamical matrix	f_0	4×10^{12} c/s
	f_1	2.73×10^{12} c/s
	f_2	0.97×10^{12} c/s
	α_1	$1.15a$
	α_2	$5a$

parameter, we use the standard definition of the screened electric field and linear dielectric constant,

$$E = E_0 + 4\pi P \approx \epsilon E_0. \quad (10)$$

After minimizing Eq. (6) in the linear, bulk limit and using the definition of the polarization from Eq. (9), we find that

$$Q = \sqrt{\frac{\mu \omega_1^2}{4\pi}(\epsilon - 1)}. \quad (11)$$

To make contact with the measured properties of the bulk material in a straightforward way, we use 90-K values for the phonon dispersion[24] and dielectric constant.[27] In terms of model parameters $\omega_1 = 2\pi(f_0 - f_1)$ and the 90-K dielectric constant are given in Table I. With this we find $Q = 8.33e$, a value comparable to those used in models of this type for bulk SrTiO$_3$.[24]

The electric field in Eq. (6) can be found by solving

$$\nabla \cdot E(z) = -\frac{4\pi e}{\epsilon_\infty} \sum_i n_i \delta(z - z_i) - 4\pi \sum_i \nabla \cdot P_i, \quad (12)$$

with the boundary conditions that $E(-\infty) = E_0$ and $E_\infty = 0$. The electric field boundary conditions are discussed below. In Eq. (12), e is the electron charge, ϵ_∞ is the high frequency dielectric constant due to electronic screening, and n_i is the number density of itinerant electrons in TiO$_2$ layer i. Both lattice relaxation and conduction band charge accumulation screen the external electric field. This is represented pictorially in Fig. 2(b).

C. Electric field boundary conditions

In the calculations presented below, we assume that the electric field above the surface of the SrTiO$_3$ has been set experimentally either by gating or by forming an interface with a polar dielectric.[26] In the latter case, E_0 is ideally set by the polarity of the material, but can also be influenced by surface reconstructions or other detailed material considerations that can be sensitive to uncontrolled aspects of growth. Because

we have gated systems in mind, we consider that E_0 can be varied experimentally over a broad range. In this calculation, we set the electric field below the SrTiO$_3$ 2DEG, E_{bulk}, to zero, assuming that the sample lies on a grounded metallic substrate. (If the SrTiO$_3$ sample was thin, a conducting layer under the sample could be used as a gate and E_{bulk} could be varied.) By integrating the Poisson equation [see Eq. (12)] and noting that the lattice relaxation contribution to $E(z)$ vanishes far below the surface when $E_{bulk} \rightarrow 0$, we conclude that the 2DEG density is fixed by E_0 alone: $n_T = \sum_i n_i = E_0/4\pi e$. We can, therefore, replace this parameter by the total 2DEG density n_T and present results as a function of that parameter.

We incorporate the layer-dependent electric potential contribution to the Hamiltonian by integrating $E(z)$ across the 2DEG to obtain a layer-dependent potential V_i, which must be determined self-consistently along with the 2DEG density-distribution and the soft-mode displacement field. With this, the Hamiltonian of the system becomes

$$H = \sum_{\langle i,j \rangle} \vec{c}_i^{\,\dagger} H^C \vec{c}_j + \sum_i \vec{c}_i^{\,\dagger}(H^{SL} + T + H^{SO} + V_i)\vec{c}_i, \quad (13)$$

where the double sum in the first term is over neighboring layers. In Eq. (13), we work in the representation $\vec{c} = \{c_{xy,\uparrow}, c_{yz,\uparrow}, c_{zx,\uparrow}, c_{xy,\downarrow}, c_{yz,\downarrow}, c_{zx,\downarrow}\}$ so that H^{SO} has the form of Eq. (5).

The layer resolved density $n_i = \langle \vec{c}_i^{\,\dagger} \vec{c}_i \rangle$ is calculated from Eqs. (12) and (13) and minimization of Eq. (6). We have carried these self-consistent field calculations to convergence over a wide range of densities for a system that is 60 unit cells wide. Because of the long tail in the density-distribution discussed at length below, it is difficult to achieve self-consistency, and we were forced to mix in no more than ~1% of new results in the iterative update of the charge density. Although the model described in this section is crude in some respects, certainly crude compared to *ab initio* electronic structure calculations with full lattice relaxation, it is strongly motivated by the cumbersome character of the fully microscopic calculations under these circumstances. The model could be made more quantitative by being bench marked against *ab initio* calculations or, perhaps more reliably, by comparison with experiment.

III. LOW-CARRIER DENSITIES 1×10^{14} cm^{-2} $< n_T$

For the circumstance considered here, the total carrier density is proportional to the electric field just above the SrTiO$_3$ surface and the largest internal electric fields are closest to the surface. We define the low-density regime by the requirement that the largest electric fields are smaller than the scale at which nonlinear screening becomes important. This field scale is set by the model parameters u_{NL} and ϵ_∞, which can be determined approximately from experiment. We have estimated u_{NL} by comparing Eq. (9) with the deviation from linear response seen in the polarization of bulk STO crystals.[27] This value is listed along with other model parameters in Table I. The model parameters we have chosen reflect the estimate that nonlinear screening becomes important for carrier densities larger than ~1×10^{14} cm^{-2}.

For linear screening, some 2DEG properties are similar to those of covalent semiconductor 2DEGs and can be estimated

following the same lines as in Stern's pioneering study of Si/SiO$_2$ MOSFET 2DEGs.[28] In particular, the confinement length scale w can be crudely estimated by equating the quantum confinement kinetic energy cost and the confinement electric potential scale. Neglecting numerical factors we, therefore, set

$$\frac{\hbar^2}{mw^2} \sim \frac{eE_0 w}{\epsilon} \sim \frac{4\pi e^2 n_T w}{\epsilon} \qquad (14)$$

to obtain

$$w \sim \left(\frac{\hbar^2 \epsilon}{4\pi m e^2 n_T}\right)^{1/3}. \qquad (15)$$

In the linear screening regime, the confinement length scale decreases quite slowly with the total 2DEG density. The hopping parameters of Table I can be converted to effective masses for the t_{2g} bands; the light mass that describes the vertical confinement of the most poorly confined $\{yz,zx\}$ bands is $\sim m_0$ where m_0 is the bare electron mass. When combined with the extremely large low-temperature bulk dielectric constant of SrTiO$_3$ ($\epsilon \sim 25\,000$), we estimate that w is close ~ 50 SrTiO$_3$ unit cells even at the top end of the low-density regime. We therefore expect that the hard wall at 60 unit cells used in our calculations influences our numerical results. The main point of these qualitative considerations is that we should expect weak surface confinement at low carrier densities because of very strong dielectric screening.

In Fig. 3, we illustrate a typical 2D band structure in the low-density regime. Here, the bottom band is beginning to reflect the increase in xy character expected from confinement, and the small size of the subband splittings is in qualitative agreement with the estimated scale of size-quantization

energies:

$$\frac{\hbar^2}{mw^2} \sim 10^{-4} \text{ eV}. \qquad (16)$$

The small subband splittings imply that the 2DEG is 3D in character unless temperatures are low and disorder extremely weak. The vertical spread of the 2DEG is expected to get smaller, and the subband splitting larger with increasing temperature as the dielectric constant value decreases.[27]

Low-carrier density properties are strongly influenced by spin-orbit coupling, which hybridizes the t_{2g} basis states and induces a splitting at the Γ point in the bulk. One effect of spin-orbit coupling is to weaken the 2DEG surface confinement by hybridizing xy bands with yz and zx bands that have smaller masses perpendicular to the surface. Spin-orbit induced hybridization allows the xy subbands to communicate between layers through their $\{yz,zx\}$ admixtures, which are less easily confined. In the low-density regime, spin-orbit splitting is pronounced enough to change the dominant orbital character of the 2D subbands.

The tetragonal distortion increases the site energy of the xy band further enhancing the role of the less confined $\{yz,zx\}$ components. (We have assumed that the tetragonal axis is parallel to the surface normal, as expected near a surface.) Initially, confinement energy scales are weak compared to the tetragonal splitting energy. As the carrier density and the energetic width of the occupied states increase, spin-orbit coupling becomes less important and the xy fraction of the lowest energy most highly occupied band increases. (See Fig. 1.) The influence of the spin-orbit and tetragonal splittings on the spatial distribution of electrons is summarized in Fig. 4. Estimating 3D densities using $n_{3D} = n_{2D}/\langle z\rangle$, where $\langle z\rangle$ is
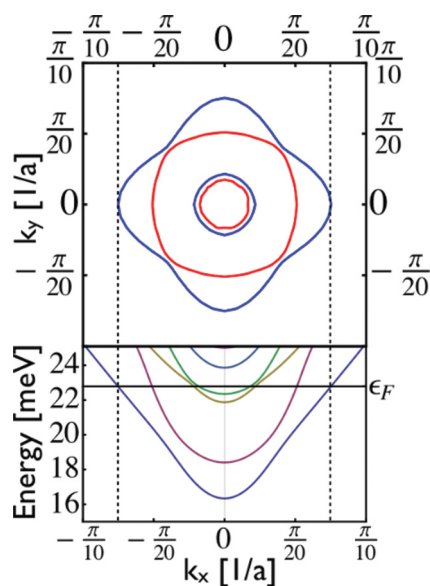

FIG. 3. (Color online) (a) Fermi surface and 2D band structure for $n_T = 8.3 \times 10^{12}$. The dominant orbital character at the 2D Γ point is represented for each band by the color of the bands and Fermi lines are blue and red for xy and $\{yz,zx\}$, respectively. The zero of energy is set to the potential minimum in the first layer. The Fermi energy is indicated by a solid (black) horizontal line.
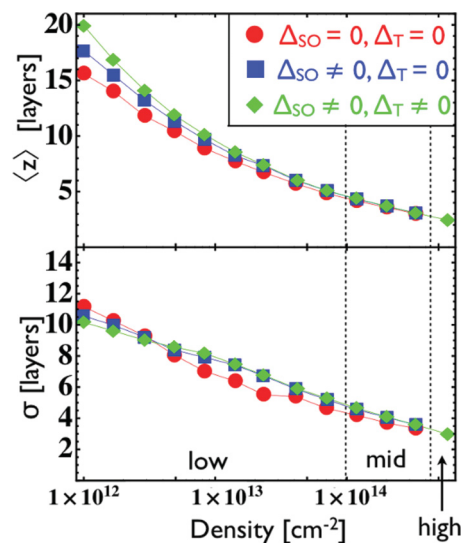

FIG. 4. (Color online) Average separation from surface, $\langle z\rangle$ and standard deviation σ of the electron distribution across layers as a function of total density, and its dependence on SO splitting and the tetragonal distortion. The tendency of SO coupling and tetragonal splitting to weaken surface confinement is suppressed when densities reach the mid range. When confinement energy scales are not strong enough to overcome the tetragonal distortion, SO and tetragonal-splitting induced hybridization decrease the spread of the $\{yz,zx\}$ bands (see text).
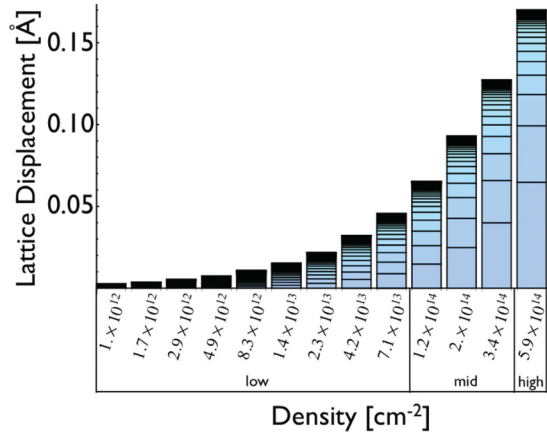
FIG. 5. (Color online) Lattice displacement as a function of total 2D density. For each density, the lattice displacement of layer i (counting from the surface) is plotted as the height of the ith bar segment (counting from the bottom). For low densities, the lattice displacements are small and in the linear regime. For mid-range densities, lattice displacements are suppressed by nonlinear screening effects near the surface. Weaker lattice screening results in stronger confinement, larger 2D subband separations, and fewer occupied 2D subbands.

taken from Fig. 4 and n_{2D} is the total density in the linear screening spatial region, we find a power law of 4/3. This suggests that the qualitative estimate of Eq. (14) is accurate when screening is linear.

IV. MID-RANGE DENSITIES: 1×10^{14} cm^{-2} < n < 5×10^{14} cm^2

We define the mid-range of densities as that in which lattice screening is markedly reduced because of nonlinear dielectric screening (see Fig. 5). Because the electric field is larger closer to the surface, nonlinear screening is more important there. The strong surface electric fields cause a large fraction of the total electron density to be confined close to the surface, and size-quantization effects to increase much more rapidly with carrier density than would be suggested by Eq. (14). Even though a substantial fraction of the total charge density starts to become confined within the top few layers, there is still a wide tail in the density distribution in the spatial region over which the external electric field has been reduced to a value less than $\sim 10^{14}$ cm$^{-2}\epsilon_{\infty}/(4\pi e)$ so that the screening is locally linear. In our model, the nonlocality of these screening properties is set by the width in momentum space of the long-wave-vector limit of the soft mode. In our numerical calculations, this low-density quasi-3D regime is influenced by our hard-wall cutoff of the 2DEG beyond a width of 60 unit cells.

As was the case in the low-density regime, the inclusion of SO coupling and the tetragonal distortion alters the the orbital character of the lowest energy band and decreases its surface confinement. Their influence is reduced compared to the low-density regime however. As illustrated in Fig. 6 we find that, at the 2D Γ point, the two lowest bands are dominantly xy in character and that the next occupied subbands are $\{yz,zx\}$ in character. Although the number of 2D subbands has increased significantly, only a few are needed to account for the most strongly confined part of the density (see the inset of Fig. 1).
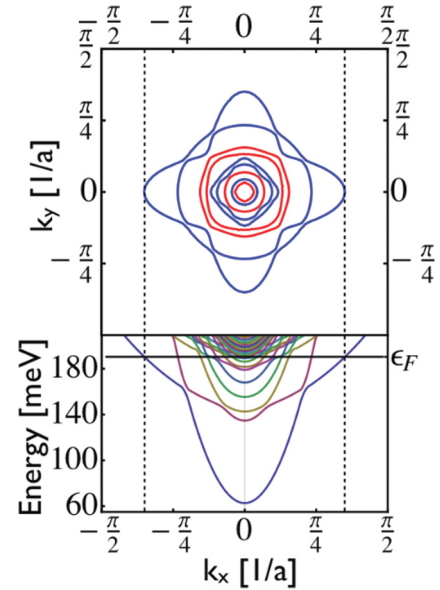

FIG. 6. (Color online) (a) Fermi surface and 2D band structure for $n_T = 2.0 \times 10^{14}$. The dominant orbital character of a band at the 2D Γ point is represented by line color with blue and red indicating xy and $\{yz,zx\}$, respectively. The zero of energy is set to the potential minimum in the first layer. The Fermi energy is represented by a solid (black) horizontal line. Although the separation between the lowest energy 2D subbands is large, many low-density subbands with small energy separations are still present near the Fermi energy.

V. HIGH-CARRIER DENSITIES: ABOVE 5×10^{14} cm^{-2}

The 2DEG electronic structure simplifies again in the high-density limit, which we define as the limit with more than half of the total density in the first TiO$_2$ layer; see Fig. 7. For large electric fields, and therefore large carrier densities,
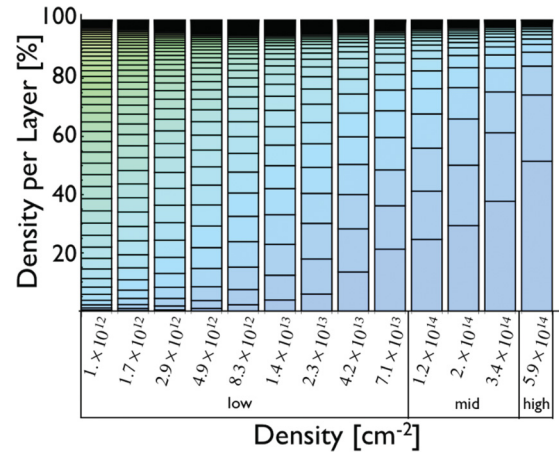

FIG. 7. (Color online) Layer resolved density (as a percent of total density) as a function of the total density. For each density each segment represents the percent of the total density in the corresponding TiO$_2$ layer, starting with the first layer and moving upward. For low densities, the 2DEG is spread over many layers. Above $n_T \sim 10^{14}$ cm^{-2}, the confinement becomes pronounced. In the high density regime, more than 50% of the total density is confined within the first layer due mainly to reduced lattice screening at large electric fields.
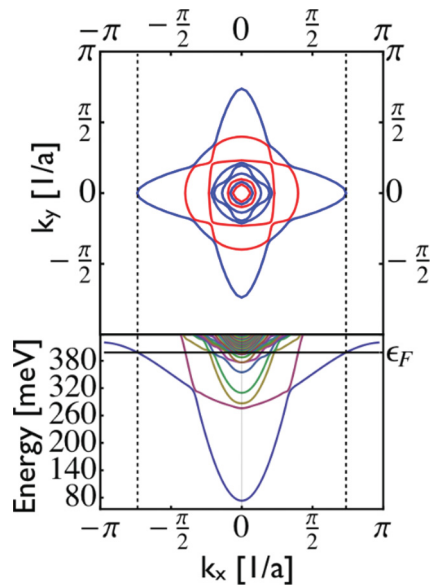
FIG. 8. (Color online) (a) Fermi surface and 2D band structure for $n_T = 5.9 \times 10^{14}$. The dominant orbital character of the band at the 2D Γ point is represented by line color with blue and red for xy and $\{yz,zx\}$, respectively. The zero of energy is set to the potential minimum in the first layer. The Fermi energy is represented by a solid (black) horizontal line. The 2D subband splitting is $\sim$200 meV— becoming comparable to the single layer model of Eq. (1). Near the Fermi energy, many subbands are present with about a milli-electron-volt splitting, which contribute to the carrier density far from the surface.

lattice screening is irrelevant near the surface. Because of the relatively large conduction band masses, compared to typical covalent semiconductor cases, and the much stronger electric fields at these carrier densities, surface confinement occurs on an atomic length scale. The Γ-point splitting becomes comparable to the single layer limit of Eq. (2); see Fig. 8. While the SO coupling leads to hybridization and a decrease in confinement that mainly affects the quasi-3D tail of the electronic distribution, the tetragonal distortion does not have a noticeable effect. In this regime, if we neglect the quasi-3D tail region, there are only a few spin-degenerate 2D subbands contributing to the density. At the 2D Γ point, the first three bands are dominantly xy and $\{yz,zx\}$—going from low to high energy. For the high-density regime, the tight-binding model of Eq. (1) must be used.

VI. SUMMARY AND DISCUSSION

Using a simplified tight-binding model for the t_{2g} bands, we find that nonlinear screening plays an essential role in determining the electronic properties of surface confined 2DEGs in grounded SrTiO₃. For low-density ($n_T < 10^{14}$ cm^{-2}) 2DEGs, electrons are distributed over many layers because surface confinement is weakened by the host material's extremely large linear dielectric constant. In the mid- and high-density regimes, a low-density tail is still present over 50 or more layers but a high-density region emerges over the first few atomic layers. Although many 2D subbands are always present in the mid- and high-density regimes, the few lowest energy
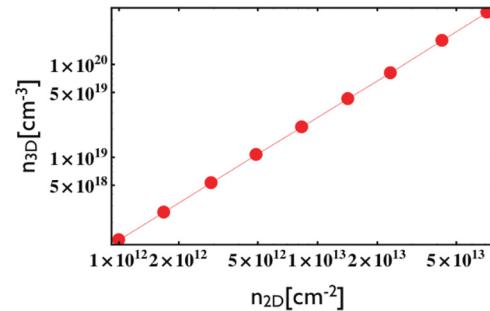

FIG. 9. (Color online) Calculated 3D density in the low density regime. The relationship between 2D density and average 3D density follows a 4/3 power law that is consistent with Eq. (14) is correct.

subbands, which contain strongly confined orbitals, account for most of the total density (see Fig. 1). Subbands that have substantial $\{yz,zx\}$ orbital character are present at all densities in the grounded configuration investigated in this study. The presence of many subbands with different orbital character at the Fermi level suggests that the interpretation of transport properties in these systems is not likely to be straightforward.

SrTiO₃ is well known for exhibiting superconductivity in the bulk[29] where it appears over a broad range of carrier densities from $\sim$10^{18} cm^{-2} to more than $\sim$10^{20} cm^{-2} and has a maximum value $\sim$400 mK.[29] In one study of gated SrTiO₃ 2DEG systems,[4] with Hall densities in the range from $\sim$10^{13} to $\sim$10^{14} cm^{-2}, the superconducting transition temperature initially increased with carrier density but decreased at the higher densities. Referencing to Fig. 9 for 3D densities associated with the weakly confined tail, we find that the measured surface 2DEG T_c's compare well with values reported for bulk systems.[29] In another study,[5] superconductivity was seen only at a Hall density of 3.9×10^{14} cm^{-2} with a transition temperature of near $\sim$400 mK. Because of experimental limitations, superconductivity was not seen at other densities but could have been present at lower transition temperatures.[5] In LaAlO₃/SrTiO₃ systems, the reported 2DEG densities are in the low-density range. It is therefore not surprising that the measured T_c values are correspondingly suppressed.[12,14] (The carriers found in LaAlO₃/SrTiO₃ 2DEG systems are thought to be induced by a polarization discontinuity, although the small value of the measured 2D carrier densities is not completely understood.) We conclude that existing studies are consistent with surface 2DEG and bulk superconductivity in SrTiO₃ having a common origin.

The strongly confined portion of the electron distribution in the mid- and high-density regimes has significant $\{yz,zx\}$ character (see Figs. 6 and 8). The increase in the density of states associated with these heavy 2D bands could account for the observed ferromagnetism,[13,14] if it is describable by a Stoner criterion. The spatial separation between the strongly confined and the low-density tail portions of the 2DEG distribution may account for the coexistence of superconductivity and magnetism seen in some systems.[14] This scenario should be compared with one in which superconductivity and magnetism both occur in strongly confined subbands; the two pictures should be experimentally distinguishable because of the strong influence of magnetism and spin-orbit coupling on superconducting properties[30] in the spatially coincident case.

The low-density tail is a consequence of the property that the electric field vanishes far from the surface of a grounded system with a surface-bound 2DEG. The nonlinear screening properties that we have discussed imply that a back-gate applied to the surface 2DEG to increase the strength of the electric field strength deep below the surface will have an exaggerated impact on the low-density tail of the distribution function and on the corresponding closely spaced 2D subbands near the Fermi surface. A gate electric field with strength $\sim 10^{14}$ cm$^{-2}\epsilon_{\infty}/4\pi e$ should essentially eliminate the tail region. Our prediction that superconductivity is associated with the low-density tail can, therefore, be tested by back gating which should suppress and eventually elimi-

nate superconductivity[7] without having a large influence on magnetism. Irrespective of the reliability of these predictions, it seems clear that studies of the electronic properties in dual-gated samples could be quite informative in building up a confident understanding of 2DEG properties.

[1] A. Ohtomo and H. Y. Hwang, Nature (London) **427**, 423 (2004).

[2] S. Thiel *et al.*, Science **313**, 1942 (2006).

[3] J. Mannhart and D. G. Schlom, Science **327**, 1607 (2010); J. Mannhart *et al.*, MRS Bulliten **33**, 1027 (2008).

[4] K. Ueno *et al.*, Nat. Mater. **7**, 855 (2008).

[5] Yeonbae Lee, Colin Clement, Jack Hellerstedt, Joseph Kinney, Laura Kinnischtzke, Xiang Leng, S. D. Snyder, and A. M. Goldman, Phys. Rev. Lett. **106**, 136809 (2011).

[6] Menyoung Lee, J. R. Williams, Sipei Zhang, C. Daniel Frisbie, and D. Goldhaber-Gordon, Phys. Rev. Lett. **107**, 256601 (2011).

[7] A. D. Caviglia *et al.*, Nature (London) **456**, 624 (2008).

[8] M. Ben Shalom, C. W. Tai, Y. Lereah, M. Sachs, E. Levy, D. Rakhmilevitch, A. Palevski, and Y. Dagan, Phys. Rev. B **80**, 140403(R) (2009); M. Salluzzo *et al.*, Phys. Rev. Lett. **102**, 166804 (2009); J. Gardner *et al.*, Nat. Phys. **7**, 895 (2011); P. R. Willmott *et al.*, Phys. Rev. Lett. **99**, 155502 (2007).

[9] M. Kim, C. Bell, Y. Kozuka, M. Kurita, Y. Hikita, and H. Y. Hwang, Phys. Rev. Lett. **107**, 106801 (2011); Y. Kozuka *et al.*, Appl. Phys. Lett. **97**, 222115 (2010); Nature (London) **462**, 7272 (2009); B. Jalan, S. Stemmer, S. Mack, and S. J. Allen, Phys. Rev. B **82**, 081103 (2010).

[10] A. Ohtomo *et al.*, Nature (London) **419**, 378 (2002); P. Moetakef *et al.*, Appl. Phys. Lett. **99**, 232116 (2011); **98**, 112110 (2011); A. F. Santander-Syro *et al.*, Nature (London) **469**, 189 (2011); W. Meevasana *et al.*, Nat. Mater. **10**, 114 (2011); M. Huijben *et al.*, arXiv:1008.1896; P. Moetakef *et al.* (unpublished).

[11] L. Li *et al.*, Science **332**, 825 (2011).

[12] N. Reyren *et al.*, Science **317**, 1196 (2007).

[13] A. Brinkman *et al.*, Nat. Mater. **6**, 493 (2007).

[14] L. Li *et al.*, Nat. Phys. **7**, 762 (2011); D. A. Dikin, M. Mehta, C. W. Bark, C. M. Folkman, C. B. Eom, and V. Chandrasekhar, Phys. Rev. Lett. **107**, 056802 (2011); J. A. Bert *et al.*, Nat. Phys. **7**, 767 (2011); P. Moetakef *et al.*, arXiv:1204.1081v1.

[15] Zoran S. Popovic, Sashi Satpathy, and Richard M. Martin, Phys. Rev. Lett. **101**, 256801 (2008).

[16] Satoshi Okamoto and Andrew J. Millis, Phys. Rev. B **70**, 075101 (2004); **70**, 241104 (2004); Z. S. Popovic and S. Satpathy, Phys. Rev. Lett. **94**, 176805 (2005); W. J. Sun, E. Cho, B. Lee, J. Lee, and S. Han, Phys. Rev. B **79**, 245411 (2009); Rossitza Pentcheva and Warren E. Pickett, Phys. Rev. Lett. **102**, 107602 (2009); Pietro Delugas, Alessio Filippetti, D. I. Bilc, D. Fontaine, and P. Ghosez, *ibid.* **106**, 166807 (2011); P. D. C. King *et al.*, *ibid.* **108**, 117602 (2012); Jaekwang Lee and Alexander A. Demkov, Phys. Rev. B **78**, 193104 (2008).

[17] Massimiliano Stengel, Phys. Rev. Lett. **106**, 136803 (2011).

[18] Reference 17 has also addressed the influence of unusual screening properties on SrTiO$_3$ 2DEGs.

[19] Y. J. Chang, A. Bostwick, Y. S. Kim, K. Horn, and E. Rotenberg, Phys. Rev. B **81**, 235109 (2010); W. Meevasana *et al.*, New J. Phys. **12**, 023004 (2010).

[20] J. S. Allen *et al.* (unpublished).

[21] L. F. Mattheiss, Phys. Rev. B **6**, 4718 (1972); D. van der Marel, J. L. M. van Mechelen, and I. I. Mazin, *ibid.* **84**, 205111 (2011); A. Janotti, D. Steiauf, and C. G. Van de Walle, *ibid.* **84**, 201304 (2011).

[22] L. F. Mattheiss, Phys. Rev. B **6**, 4740 (1972); H. Uwe *et al.*, Jpn. J. Appl. Phys. **24**, 335 (1985); **24**, 519 (1985).

[23] R. Bistritzer, G. Khalsa, and A. H. MacDonald, Phys. Rev. B **83**, 115114 (2011).

[24] R. A. Cowley, Phys. Rev. **134**, A981 (1964).

[25] Y. Yamada and G. Shirane, J. Phys. Soc. Jpn. **26**, 369 (1969).

[26] N. Nakagawa, H. Y. Hwang, and D. A. Muller, Nat. Mater. **5**, 204 (2006).

[27] R. C. Neville *et al.*, J. Appl. Phys. **43**, 2124 (1972).

[28] F. Stern, Phys. Rev. B **5**, 4891 (1972).

[29] J. F. Schooley *et al.*, Phys. Rev. Lett. **14**, 305 (1965); C. S. Koonce *et al.*, Phys. Rev. **163**, 380 (1967).

[30] K. Michaeli, A. C. Potter, and P. A. Lee, Phys. Rev. Lett. **108**, 117003 (2012).